Physics Letters A 381 (2017) 2709–2714

Contents lists available at ScienceDirect

Physics Letters A

www.elsevier.com/locate/pla

Exchange bias study of sub-100 nm-diameter CoFeB/IrMn antidot and nanodot arrays fabricated by nanosphere lithography

X. Li [a], C.W. Leung [b], C.-C. Chiu [c], K.-W. Lin [c,*], Mansun Chan [d], Y. Zhou [e], Philip W.T. Pong [a,*]

[a] Department of Electrical and Electronic Engineering, The University of Hong Kong, Hong Kong
[b] Department of Applied Physics, The Hong Kong Polytechnic University, Hong Kong
[c] Department of Materials Science and Engineering, National Chung Hsing University, Taichung 402, Taiwan
[d] Department of Electronic and Computer Engineering, Hong Kong University of Science and Technology, Hong Kong
[e] School of Science and Engineering, The Chinese University of Hong Kong, Shenzhen, 518172, China

ARTICLE INFO

Article history:
Received 29 December 2016
Received in revised form 16 May 2017
Accepted 5 June 2017
Available online 12 June 2017
Communicated by M. Wu

Keywords:
Exchange bias
Nanostructures
Nanosphere lithography

ABSTRACT

Exchange-coupled bilayers are widely used as pinned layers in nanometric spintronic devices. In this work, sub-100 nm-diameter CoFeB/IrMn antidot and nanodot arrays were patterned by nanosphere lithography. The exchange bias (H_{ex}) and coercivity (H_c) of the nanostructures and continuous films exhibit similar exponential dependence on CoFeB layer thickness. Magnetic field annealing results in changed crystallinity, surface roughness, and magnetic properties. Reduced H_c and enhanced H_{ex} are observed after annealing at low temperatures, while high-temperature annealing results in higher H_c and lower H_{ex}. This work provides physical insights on the magnetization reversal response in nanosized spintronic devices involving CoFeB/IrMn reference layers.

© 2017 Elsevier B.V. All rights reserved.

1. Introduction

The centers of hysteresis loops of ferromagnetic (FM) thin films shift away from zero when interfacing with antiferromagnetic (AF) layers [1]. This phenomenon is broadly known as the exchange bias effect. Benefited from the enhanced coercivity (H_c) and the loop shift (H_{ex}) [2], the exchange bias effect has brought great flexibility in tailoring the magnetization reversal properties of the reference layers in spin valves [3,4]. Ever since the primary discovery in CoO coated Co particles [5], intense research have been conducted to reveal the influencing factors of exchange bias, such as thin film composition [6,7], layer thickness [6,8], applied field angle [9], field cooling [10,11], ion-beam bombardment [12], and post annealing [13,14].

The emergence of state-of-the-art micro- and nano-fabrication techniques accelerate the research and development on various nanostructures such as nanodot and antidot arrays. The nanopatterned dot structures are widely used in spintronic devices such as the nanometric magnetoresistive sensors [15], magnetic random access memories [16], and spin torque oscillators [17]. The patterned nanodot and antidot arrays can also be potentially used in high-density magnetic storage [18]. Since the domain structures [19] and grain size distributions [20] are altered by the reduced structural size, the exchange interactions in nanostructures differ greatly from those in continuous films [21,22]. Both enhanced and reduced H_{ex} in nanostructures is reported, depending on the AF layer thicknesses [23–25] and structural sizes [26]. Most of the previous reports focus on the exchange-biased nanostructures with polycrystalline structures (such as CoFe/IrMn [21] and Co/IrMn [27]). CoFeB is an amorphous FM material which is widely used in magnetic tunnel junctions [28]. Both positive [29] and negative [30] H_{ex} are reported in CoFeB/IrMn planar films. However, the dependence of H_{ex} and H_c on CoFeB thickness in CoFeB/IrMn nanostructures remain unclear. Besides, CoFeB is partially crystallized after annealing [31], which may also result in changes in H_{ex} and H_c. The investigation on the magnetic properties and annealing effect of CoFeB/IrMn nanostructures will be beneficial for understanding the magnetic switching properties in nanometric spintronic devices.

Nanosphere lithography (NSL) is a promising nanofabrication technique with advantages including high yield, flexibility in size control, and low cost. Unlike the conventional electron beam lithography method which takes time in pumping down the system and being a serial process in nature, this method is a parallel process, and it only takes several minutes to distribute wide-area sphere masks. The size of nanostructures can also be tailored by

* Corresponding authors.
E-mail addresses: kwlin@dragon.nchu.edu.tw (K.-W. Lin), ppong@eee.hku.hk (P.W.T. Pong).

http://dx.doi.org/10.1016/j.physleta.2017.06.010
0375-9601/© 2017 Elsevier B.V. All rights reserved.

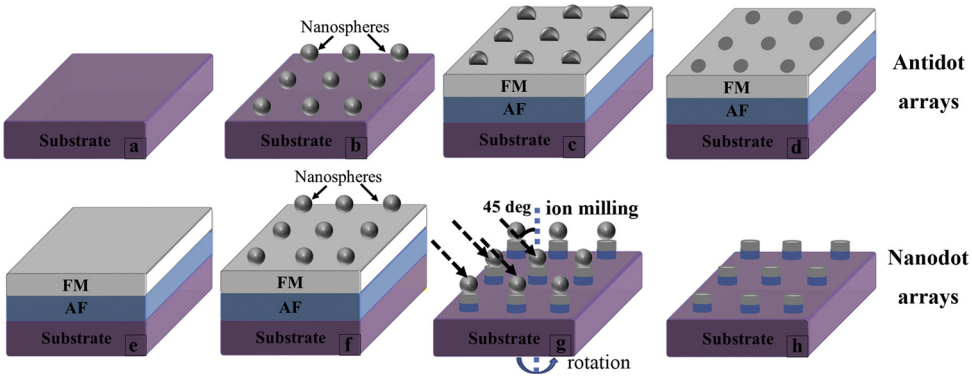

Fig. 1. Fabrication processes of antidot arrays ((a)–(d)) and nanodot arrays ((e)–(h)).

simply varying the ion-milling tilt angles without the need of a new photomask, which offers flexibility in size control compared with UV photolithography. In addition, this method only engages common laboratories apparatus such as beakers and pipettes. All these characteristics make it a low-cost straight-forward method for fabricating nanostructures with high-throughput large-area patterning, which is necessary for this kind of nanomagnetism research. The recent demonstration of magnetic nanodot [32–37], antidot [38–40], spin valve nanopillars [41], and spin-torque oscillators [42] fabricated by NSL have proved its feasibility in patterning nanostructures for investigating magnetic properties. In this work, NSL was engaged for parallel fabrication of large-area CoFeB/IrMn nanodot and antidot arrays with diameters of less than 100 nm. The magnetic properties of continuous films, antidot, and nanodot arrays were compared and analyzed to study the influence of FM-layer thickness and annealing effect.

2. Material and methods

The layer stack is Si/SiO_2/Ta 3.5/Ru 3.5/IrMn 8/CoFeB t_{FM}/Ta 3.5 (thickness in nanometers), in which t_{FM} is adjusted from 2 to 10 nm. High purity Ta, Cu, $Ir_{20}Mn_{80}$, $Co_{40}Fe_{40}B_{20}$, and Ru targets were DC-sputtered in argon pressure of 3×10^{-3} Torr at deposition rates ranging from 0.4 to 1 nm/min. An in-plane magnetic field of 30 mT was applied during the deposition.

The patterning processes of nanodot and antidot arrays are similar to that in the references [32,39,43]. Detailed fabrication steps are shown in Fig. 1. For the antidot arrays, the substrates were firstly cleaned and treated with positive electrolyte (0.2% water solution of Poly(diallyldimethylammonium chloride)) (Fig. 1(a)). Non-close-packed polystyrene nanospheres (120 nm, negatively charged) were adsorbed to the wafer surface (Fig. 1(b)) by electrostatic interaction. Thin film stacks were subsequently deposited on the sphere masks while the substrate was rotating at 40 rpm ((Fig. 1(c)). The antidot arrays were formed (Fig. 1(d)) by lifting-off the spheres in toluene. For the nanodot arrays, the continuous films were firstly deposited onto the rotating substrate (Fig. 1(e)). Then nanospheres were adsorbed to the film surface (Fig. 1(f)). Ar^+ ion milling was conducted while the sample was spinning at 37 rpm (Fig. 1(g)). Since the ion beam was tilted by 45 degrees, the diameters of the nanodots were smaller than that of the spheres. Each sample was etched for 3 minutes at an overall etching rate of around 10 nm/min (the etching rate varies depending on the material). The nanodot arrays were formed by removing the residual spheres in toluene (Fig. 1(h)).

Samples with $t_{FM} = 6$ nm were vacuum annealed for 60 minutes under magnetic field of 0.15 T at 373 K to 673 K to investigate the annealing effect. The room-temperature magnetization hysteresis loops of the as-deposited and annealed samples were measured between −0.4 T and 0.4 T by a Microsense EZ7 vibrating sample

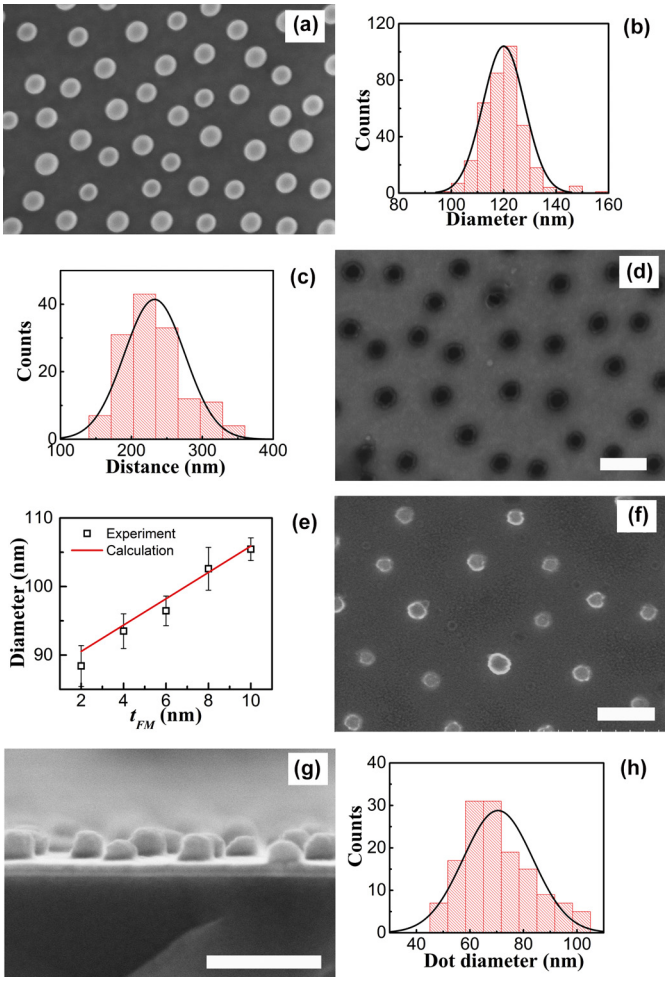

Fig. 2. The surface morphologies of the samples characterized by SEM. (a) planar view of the nanospheres adsorbed on wafer surface; (b) the distribution histogram of the diameter of nanospheres; (c) the distribution histogram of the center-to-center distance between the adjacent antidots; (d) planar view of the antidot arrays with $t_{FM} = 8$ nm; (e) square dot: the measured pore diameter (scale bar refers to the 95% confidence interval of 30 samples); solid line: the calculated pore diameter based on the thin film thickness and sphere diameter); (f) planar view of the nanodot arrays with $t_{FM} = 2$ nm; (g) cross-sectional view of the nanodot arrays with $t_{FM} = 2$ nm (h) the distribution histogram of the diameter of nanodots. (Scale bar represents 200 nm. The histograms in (b), (c) and (h) are acquired through measuring the diameter and distance on SEM images. 80–361 measurements were conducted in each histogram.) (For interpretation of the references to color in this figure legend, the reader is referred to the web version of this article.)

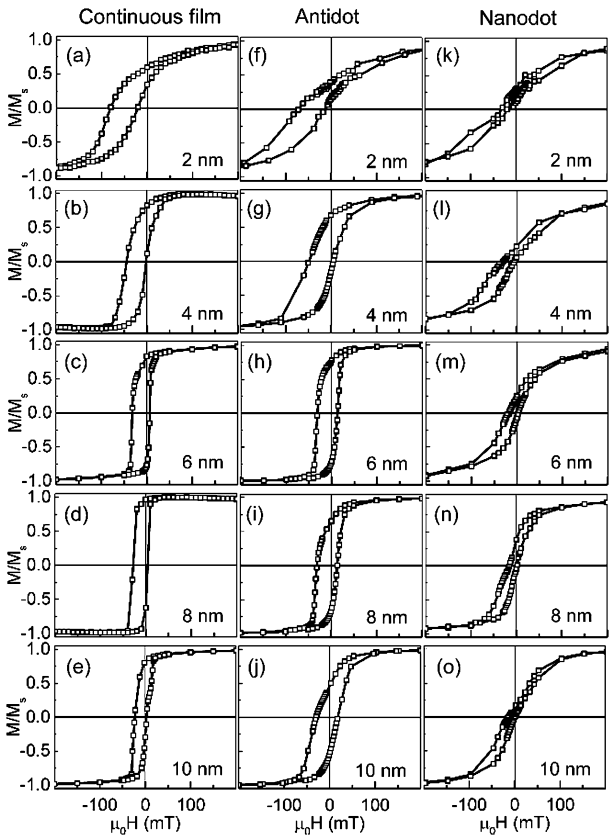

Fig. 3. The magnetic hysteresis loops of continuous films ((a)–(e)), antidot ((f)–(j)) and nanodot arrays ((k)–(o)) at different t_{FM}.

magnetometer (VSM). The direction of the magnetic field during deposition and annealing were parallel to the positive direction of the VSM measurement. The planar and cross-sectional images were observed by a Hitachi S4800 field-emission scanning electron microscope (FE-SEM). The crystalline structures of the planar films were characterized by a Brüker AXS D8 Advance grazing incidence (0.5 degrees) X-ray diffraction (GIXRD) spectrometer. The surface morphologies of the planar films were characterized by a Parker XE-150 atomic force microscope (AFM) operating in tapping mode.

3. Results and discussions

The surface morphologies of the samples are shown in Fig. 2. Non-close-packed spheres are uniformly distributed (Fig. 2(a)) with an average diameter of 120 ± 1 nm (Fig. 2(b)) and an average center-to-center distance of 240 ± 2 nm (Fig. 2(c)). The planar view of antidot arrays with $t_{FM} = 8$ nm is presented in Fig. 2(d). The radial distribution of the antidots duplicates that of the nanosphere masks. Due to the spherical shape of the mask, the diameter of pores in the antidot arrays are smaller than that of the nanospheres. The material gradually fills up the spaces amongst the spheres, resulting in increasing pore diameter with thin film thickness, as shown in Fig. 2(e). The top and cross-sectional views of the nanodot arrays are shown in Figs. 2(f) and 2(g), respectively. The diameter of the dots with $t_{FM} = 2$ nm is reduced to 70 ± 3 nm (Figs. 2(h)) in the tilted ion milling process. The 30-nm-thick dots observed by SEM are composed of multilayer stacks ($t = 20.8$ nm–28.5 nm) and the over-etched substrate.

From the morphologies of the samples, we can conclude that regular nanostructures with lateral dimensions down to 70 nm can be fabricated by NSL. Based on this new method, the magnetic properties of CoFeB/IrMn exchange-biased nanostructures were investigated. The hysteresis loops of the patterned nanostructures are

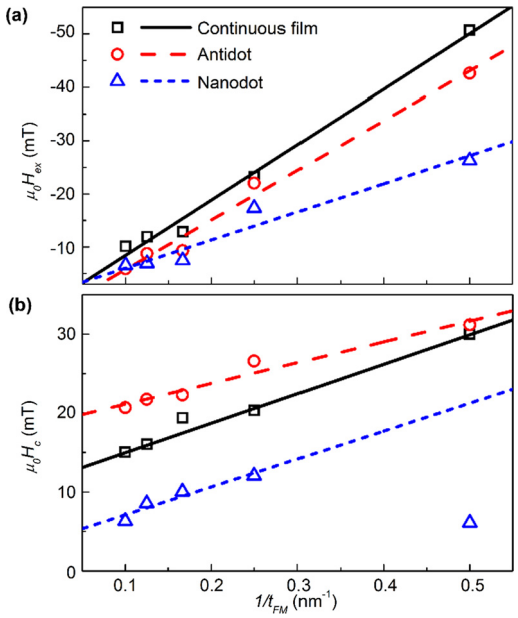

Fig. 4. (a) H_{ex} and (b) H_c as a function of t_{FM} in continuous films, antidot and nanodot arrays respectively.

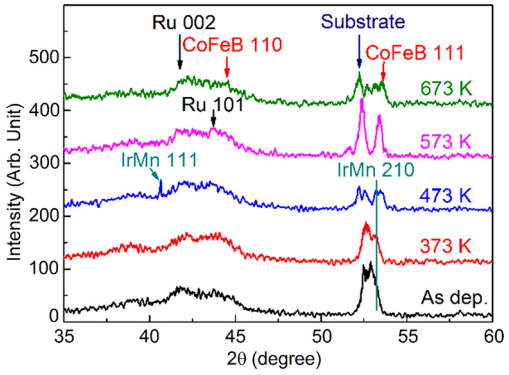

Fig. 5. GIXRD patterns of the as-deposited and field-annealed continuous films.

more curved and less square than those of the continuous films (Fig. 3), due to the pinning effect of edges and defects in nanostructures. The high symmetricity in the loops of nanodot arrays evidences that the interdot magnetostatic coupling is not present [44]. With increasing t_{FM}, the magnetic hysteresis loops of nanodot array exhibit enhanced squareness and reduced loop shift. This is because the field-induced magnetic anisotropy incurred during deposition makes a greater contribution than the exchange anisotropy.

The H_{ex} and H_c of continuous films and nanostructures are plotted against $1/t_{FM}$ in Figs. 4(a) and 4(b), respectively. As predicted by Stiles et al. [45–47], the H_{ex} and H_c of the continuous films exhibit exponential reliance on the FM thickness (t_{FM}):

$$H_{ex} \propto \frac{1}{t_{FM}^{m}} \tag{1}$$

$$H_c \propto \frac{1}{t_{FM}^{n}} \tag{2}$$

where m and n are positive numbers, and approaches unity at room temperature. This relation is already reported in many experimental investigations on polycrystalline FM/AF pairs (such as Fe/MnF_2 [2], CoFe/IrMn [48], NiFe/FeMn [49] and NiFe/NiO [49]). The results in Fig. 4 proves that H_{ex} and H_c of the continuous films and nanostructures of amorphous-CoFeB/IrMn also follow

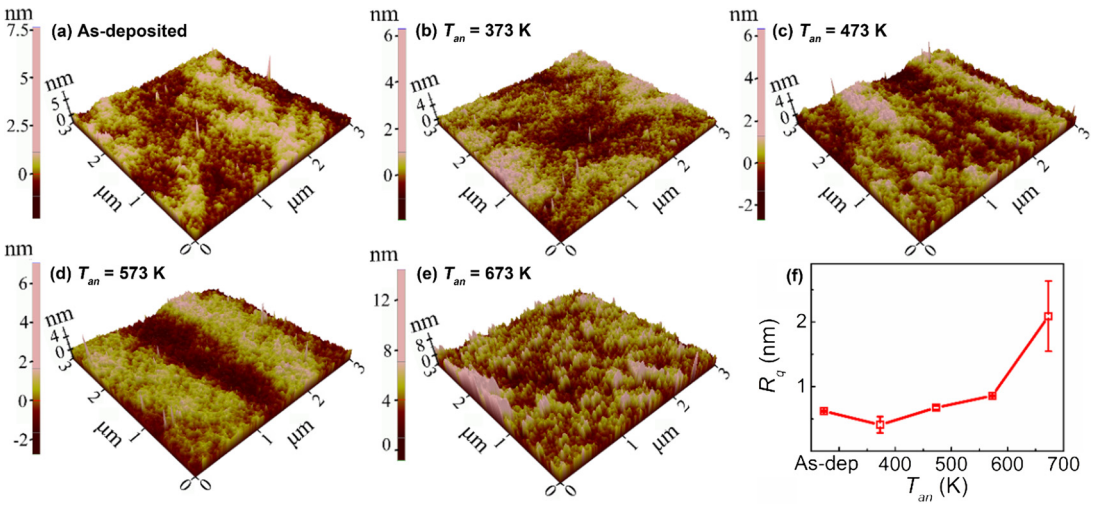

Fig. 6. (a)–(e) AFM images (3 μm×3 μm) and (f) RMS roughness measured on as-deposited and field annealed planar films. (The error bars refer to the standard deviation of R_q measured on three regions.)

this $1/t_{FM}$ relation. It is noted that the H_c of the nanodot arrays shows some deviations from the linear fitting when $t_{FM} = 2$ nm. The small H_c for the thin nanodot is attributed to the fact that the anisotropy barrier decreases with thin film thickness [50]. So, smaller magnetic field is required to reverse the magnetization of thin nanodot with the assistance of thermal energy. The H_{ex} of the antidot arrays are smaller than that of the continuous films, which is contradictory to some previous observations [25]. However, this phenomenon can be explained by the misaligned FM and AF spins at the edges of the pores [51]. In the meantime, the effect of reduced AF domain size, which is responsible for the enhance H_{ex} in antidot structures in the previous report [52], becomes marginal as the diameters of the antidots are reduced to smaller than 100 nm. Indeed, H_{ex} decreases at smaller pore diameter in NiFe/IrMn antidot arrays, as reported in the reference [53]. The smaller H_{ex} in nanodot arrays, on the other hand, is consistent with the previous report on 50-nm Co/IrMn nanodots [54]. The H_c of antidot arrays is larger than that of the continuous films, due to the enhanced domain wall pinning at the edge of the nanostructures in the FM and AF layers [21,55]. It is possible that the observed changes in H_{ex} and H_c at larger t_{FM} may also be influenced by the increased pore diameter in the antidot arrays. However, according to the previous report [56] and our micromagnetic simulation (supplementary information), the size-induced changes are much smaller compared with the experimentally measured H_{ex} and H_c variation at different t_{FM}, indicating the thickness dependence plays a dominant role over the size effect. The H_c of the nanodot array is smaller than that of the continuous film. This difference is consistent with the previous report on Co/CoO nanodot arrays that H_{ex} and H_c decrease with reducing diameter [44]. This is possibly because of the reduction in thermal stability in the sub-100 nm-diameter nanodots.

Magnetic field annealing was conducted at varied temperatures to further modify the microstructure and magnetic properties of the films and nanostructures. In order to investigate the structural changes induced by field annealing, the GIXRD patterns of as-deposited and annealed continuous films are shown in Fig. 5. The surface morphologies and root mean square (RMS) roughness (R_q) at different T_{an} are shown in Fig. 6. The as-deposited sample presents two broadened peaks at $2\theta = 42.2°$ and 44.1°, corresponding to Ru (002) and (101) grains, respectively. The major peak at $2\theta = 53°$ can be decomposed into one sub-peak at $2\theta = 52.5°$ (which comes from the Si/SiO_2 substrate [57]) and another one at $2\theta = 54°$ (which is contributed by IrMn (210)). When annealed at 473 K, a sharp IrMn (111) peak emerges at $2\theta = 41.4°$, indicating remarkable enhancement of crystallinity of IrMn. The recrystallization process relaxes the structural defects and disorders during the low-temperature annealing, resulting in the slight decrease in roughness in Fig. 6. No diffraction peak of CoFeB crystallite is observed at T_{an} below 473 K, which confirms the amorphous structure of as-deposited CoFeB layer. Further increasing T_{an} results in body-centered cubic (BCC) CoFeB (111) texture, which is consistent with the previous report on the annealed CoFeB/Ru multilayers [58]. Meanwhile, the diffraction peaks of IrMn gradually vanishes, due to the detrimental effect of Boron and Mn interdiffusion at high annealing temperatures [59,60]. When $T_{an} = 673$ K, the broad diffused peak centered at $2\theta = 45°$ indicates the formation of CoFeB (110) grains. The crystallization of CoFeB results in non-uniformly distributed spikes on the sample surface, which is responsible for the large standard deviation of the measured R_q. The crystallization [61,62] and interdiffusion [63] also result in a gradual increase in R_q with T_{an}.

The changes in phases and structures in CoFeB/IrMn bilayers after annealing altered the magnetic properties of the continuous films, antidot and nanodot samples, as shown in Fig. 7. The squareness of the hysteresis loops is increased after 373 K annealing. This is because the density of defects in CoFeB is reduced after 373 K annealing, as evidenced by the lower roughness characterized by AFM. The CoFeB layer switches more homogeneously when fewer pinning sites exist. Further increasing T_{an} results in reduced squareness because the domain wall motion is pinned by the diffused Mn atoms and the magnetization reversal mechanism is dominated by the rotation of interfacial magnetization [64].

The H_{ex} and H_c of the antidot and nanodot arrays follow similar reliance on T_{an} as the continuous films (Fig. 8). The annealing temperature dependence of H_{ex} is closely correlated to the IrMn crystallinity shown in Fig. 5. When $T_{an} < 473$ K, the H_{ex} increases with T_{an} due to the enhanced AF ordering in IrMn. The enhanced H_{ex} when $T_{an} = 373$ K results in slightly increased H_c. With increasing T_{an}, the H_{ex} is remarkably reduced due to the loss of polycrystalline ordering in IrMn after high-temperature annealing. However, small H_c is observed when T_{an} is increased to 473 K or 573 K. The coexistence of high H_{ex} and low H_c when $T_{an} = 473$ K is attributed to the diffusion of Mn in CoFeB/IrMn interface. The diffusion-induced uncompensated interfacial spins in IrMn contributes to higher H_{ex} [30], while the diluted magnetic interface in CoFeB leads to lower H_c [29]. When $T_{an} = 673$ K, due to the crystallization of CoFeB, H_{ex} reaches minimum while H_c reaches maximum. The above results show that magnetic field annealing is

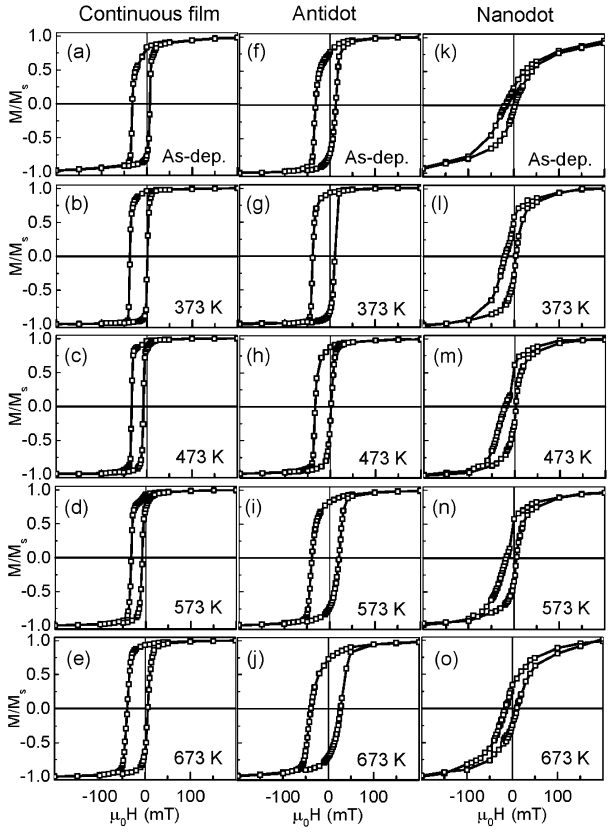

Fig. 7. The magnetization hysteresis loops of as-deposited and field annealed continuous films ((a)–(e)), antidot ((f)–(j)) and nanodot arrays ((k)–(o)) of CoFeB/IrMn exchange bias system with $t_{FM} = 6$ nm.

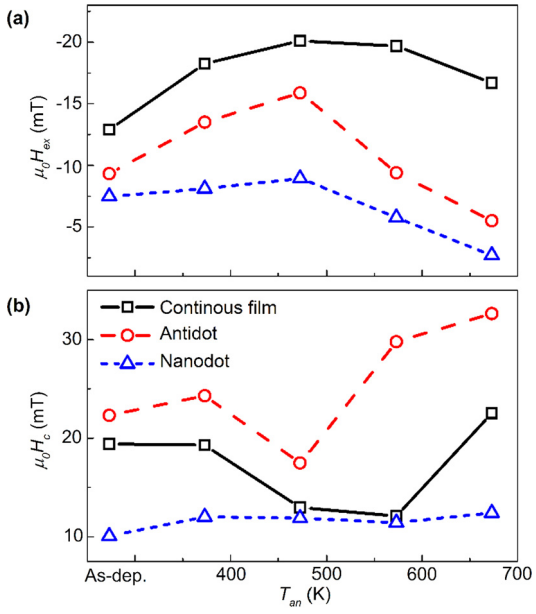

Fig. 8. (a) H_{ex} and (b) H_c of the continuous films, antidot arrays, and nanodot arrays as a function of T_{an} when $t_{FM} = 6$ nm.

effective in tailoring the microstructures and magnetic properties of exchange-biased multilayers.

4. Conclusions

The thickness dependence and annealing effect of the magnetic properties of CoFeB/IrMn continuous films and sub-100-nm-diameter nanostructures were investigated. The H_{ex} and H_c of the antidot arrays, nanodot arrays, and continuous films demonstrate similar $1/t_{FM}$ reliance on the amorphous-FM layer thickness as in polycrystalline multilayers. Field annealing at low temperature ($T_{an} < 473$ K) enhances the crystallization of IrMn, resulting in higher H_{ex}. Interdiffusion is promoted at the higher annealing temperature, which leads to reduced IrMn crystallinity, increased surface roughness, and reduced H_{ex}. Both enhanced and reduced H_c are observed depending on T_{an}, due to the competing effect of exchange interaction and CoFeB crystallization (which increases H_c) and Mn diffusion (which reduces H_c). The results show that the exponential thickness dependence of H_{ex} and H_c can be extended to sub-100 nm-diameter nanostructures of amorphous-FM/AF bilayers. This work provides useful insight and guidance for the magnetic properties and microstructures of nanoscale spintronic devices containing CoFeB/IrMn reference layers.

Acknowledgement

This research is supported by the Seed Funding Program for Basic Research, Seed Funding Program for Applied Research and Small Project Funding Program from the University of Hong Kong, ITF Tier 3 funding (ITS-104/13,ITS-214/14), and University Grants Committee of HK (AoE/P-04/08). X.L. acknowledges Nanosystem Fabrication Facility (NFF) of HKUST for the device characterization. C.W.L. acknowledges the support by The Hong Kong Polytechnic University (G-YBPU/G-YBJ1/1-ZVGH). Y.Z. acknowledges support by the National Natural Science Foundation of China (Project No. 11574137) and Shenzhen Fundamental Research Fund under Grant No. JCYJ20160331164412545.

Appendix A. Supplementary material

Supplementary material related to this article can be found online at http://dx.doi.org/10.1016/j.physleta.2017.06.010.

References

[1] J. Nogués, I.K. Schuller, J. Magn. Magn. Mater. 192 (1999) 203.
[2] C. Leighton, M.R. Fitzsimmons, A. Hoffmann, J. Dura, C.F. Majkrzak, M.S. Lund, I.K. Schuller, Phys. Rev. B 65 (2002) 064403.
[3] I.L. Prejbeanu, S. Bandiera, J. Alvarez-Hérault, R.C. Sousa, B. Dieny, J.P. Nozières, J. Phys. D, Appl. Phys. 46 (2013) 074002.
[4] C. Zheng, R.D. Shull, P.J. Chen, P.W.T. Pong, Phys. Lett. A 380 (2016) 2237–2241.
[5] W.H. Meiklejohn, C.P. Bean, Phys. Rev. 105 (1957) 904–913.
[6] Jing-guo Hu, Guo-jun Jin, Y.-q. Ma, J. Appl. Phys. 92 (2002) 1009–1013.
[7] X. Li, K.W. Lin, W.C. Yeh, R.D. Desautels, J. van Lierop, P.W.T. Pong, Phys. Lett. A 381 (2017) 524–528.
[8] M. Ali, C.H. Marrows, M. Al-Jawad, B.J. Hickey, A. Misra, U. Nowak, K.D. Usadel, Phys. Rev. B 68 (2003) 214420.
[9] T. Ambrose, R.L. Sommer, C.L. Chien, Phys. Rev. B 56 (1997) 83.
[10] K.W. Lin, M.R. Wei, J.Y. Guo, J. Nanosci. Nanotechnol. 9 (2009) 2023.
[11] X. Li, K.W. Lin, H.Y. Liu, D.H. Wei, G.J. Li, P.W.T. Pong, Thin Solid Films 570 (2014) 383–389.
[12] K.W. Lin, M. Mirza, C. Shueh, H.R. Huang, H.F. Hsu, J. van Lierop, Appl. Phys. Lett. 100 (2012) 122409.
[13] A.C. Sun, H.F. Hsu, H.J. Wu, J.H. Hsu, P.W.T. Pong, T. Suzuki, K.W. Lin, IEEE Trans. Magn. 47 (2011) 501.
[14] T. Yu, H. Naganuma, W.X. Wang, Y. Ando, X.F. Han, J. Appl. Phys. 111 (2012) 07D908.
[15] I. Will, A. Ding, Y. Xu, J. Magn. Magn. Mater. 388 (2015) 5–9.
[16] E. Chen, D. Apalkov, Z. Diao, A. Driskill-Smith, D. Druist, D. Lottis, V. Nikitin, X. Tang, S. Watts, S. Wang, S.A. Wolf, A.W. Ghosh, J.W. Lu, S.J. Poon, M. Stan, W.H. Butler, S. Gupta, C.K.A. Mewes, T. Mewes, P.B. Visscher, IEEE Trans. Magn. 46 (2010) 1873–1878.
[17] R.K. Dumas, S.R. Sani, S.M. Mohseni, E. Iacocca, Y. Pogoryelov, P.K. Muduli, S. Chung, P. Durrenfeld, J. Akerman, IEEE Trans. Magn. 50 (2014) 4100107.
[18] R. Morales, M. Kovylina, I.K. Schuller, A. Labarta, X. Batlle, Appl. Phys. Lett. 104 (2014) 032401.
[19] A. Fraile Rodríguez, A.C. Basaran, R. Morales, M. Kovylina, J. Llobet, X. Borrisé, M.A. Marcus, A. Scholl, I.K. Schuller, X. Batlle, A. Labarta, Phys. Rev. B 92 (2015) 174417.

[20] V. Baltz, G. Gaudin, P. Somani, B. Dieny, Appl. Phys. Lett. 96 (2010) 262505.
[21] M.T. Rahman, N.N. Shams, D.S. Wang, C.-H. Lai, Appl. Phys. Lett. 94 (2009) 082503.
[22] A. Sharma, S. Tripathi, K.C. Ugochukwu, J. Magn. Magn. Mater. 326 (2013) 97.
[23] V. Baltz, J. Sort, S. Landis, B. Rodmacq, B. Dieny, Phys. Rev. Lett. 94 (2005) 117201.
[24] W.J. Gong, W. Liu, J.N. Feng, D.S. Kim, C.J. Choi, Z.D. Zhang, J. Appl. Phys. 115 (2014) 133909.
[25] D. Tripathy, A.O. Adeyeye, J. Appl. Phys. 105 (2009) 07D703.
[26] K. Temst, E. Girgis, R.D. Portugal, H. Loosvelt, E. Popova, M.J.V. Bael, C.V. Haesendonck, H. Fritzsche, M. Gierlings, L.H.A. Leunissen, R. Jonckheere, Eur. Phys. J. B 45 (2005) 261.
[27] G. Vinai, J. Moritz, G. Gaudin, J. Vogel, M. Bonfim, F. Lançon, I.L. Prejbeanu, K. Mackay, B. Dieny, J. Phys. D, Appl. Phys. 46 (2013) 345308.
[28] S. Ikeda, J. Hayakawa, Y. Ashizawa, Y.M. Lee, K. Miura, H. Hasegawa, M. Tsunoda, F. Matsukura, H. Ohno, Appl. Phys. Lett. 93 (2008) 082508.
[29] M. Raju, S. Chaudhary, D.K. Pandya, Eur. Phys. J. B 86 (2013) 491.
[30] A. Kohn, J. Dean, A. Kovacs, A. Zeltser, M.J. Carey, D. Geiger, G. Hrkac, T. Schrefl, D. Allwood, J. Appl. Phys. 109 (2011) 083924.
[31] S. Yuasa, Y. Suzuki, T. Katayama, K. Ando, Appl. Phys. Lett. 87 (2005) 242503.
[32] L. Balcells, B. Martinez, O. Iglesias, J.M. García-Martín, A. Cebollada, A. García-Martín, G. Armelles, B. Sepúlveda, Y. Alaverdyan, Appl. Phys. Lett. 94 (2009) 062502.
[33] J.B. González-Díaz, A. García-Martín, J.M. García-Martín, A. Cebollada, G. Armelles, B. Sepúlveda, Y. Alaverdyan, M. Käll, Small 4 (2008) 202.
[34] S.M. Weekes, F.Y. Ogrin, W.A. Murray, P.S. Keatley, Langmuir 23 (2006) 1057.
[35] X. Li, Z.R. Tadisina, S. Gupta, G. Ju, J. Vac. Sci. Technol. A 27 (2009) 1062–1066.
[36] P. Tiberto, G. Barrera, L. Boarino, F. Celegato, M. Coisson, N. De Leo, F. Albertini, F. Casoli, P. Ranzieri, J. Appl. Phys. 113 (2013) 17B516.
[37] P. Tiberto, L. Boarino, F. Celegato, M. Coisson, E. Enrico, N. de Leo, F. Vinai, P. Allia, J. Nanopart. Res. 13 (2011) 4211.
[38] M. Coïsson, L. Boarino, F. Celegato, N. Leo, P. Tiberto, F. Vinai, J. Nanopart. Res. 13 (2011) 5641.
[39] C.-C. Ho, T.-W. Hsieh, H.-H. Kung, W.-T. Juan, K.-H. Lin, W.-L. Lee, Appl. Phys. Lett. 96 (2010) 122504.
[40] P. Tiberto, L. Boarino, F. Celegato, M. Coisson, N. De Leo, F. Vinai, P. Allia, J. Appl. Phys. 107 (2010) 09B502.
[41] W.G. Wang, A. Pearse, M. Li, S. Hageman, A.X. Chen, F.Q. Zhu, C.L. Chien, Sci. Rep. UK 3 (2013) 01948.
[42] B. Fang, J. Feng, H. Wei, X. Han, B. Zhang, Z. Zeng, J. Nanomater 2015 (2015) 6.
[43] P. Hanarp, D.S. Sutherland, J. Gold, B. Kasemo, Colloids Surf. A, Physicochem. Eng. Asp. 214 (2003) 23–36.
[44] E. Girgis, R.D. Portugal, H. Loosvelt, M.J. Van Bael, I. Gordon, M. Malfait, K. Temst, C. Van Haesendonck, L.H.A. Leunissen, R. Jonckheere, Phys. Rev. Lett. 91 (2003) 187202.
[45] M.D. Stiles, R.D. McMichael, Phys. Rev. B 60 (1999) 12950.
[46] M.D. Stiles, R.D. McMichael, Phys. Rev. B 59 (1999) 3722–3733.
[47] M.D. Stiles, R.D. McMichael, Phys. Rev. B 63 (2001) 064405.
[48] H. Li, P.P. Freitas, Z. Wang, J.B. Sousa, P. Gogol, J. Chapman, J. Appl. Phys. 89 (2001) 6904.
[49] T. Lin, T. Ching, R.E. Fontana, J.K. Howard, IEEE Trans. Magn. 31 (1995) 2585.
[50] I. Tudosa, M.V. Lubarda, K.T. Chan, M.A. Escobar, V. Lomakin, E.E. Fullerton, Appl. Phys. Lett. 100 (2012) 102401.
[51] J. Changjun, X. Desheng, F. Xiaolong, G. Dangwei, L. Qingfang, Nanotechnology 18 (2007) 335703.
[52] A.P. Malozemoff, Phys. Rev. B 35 (1987) 3679–3682.
[53] D. Tripathy, A.O. Adeyeye, N. Singh, Appl. Phys. Lett. 93 (2008) 022502.
[54] G. Vinai, J. Moritz, G. Gaudin, J. Vogel, M. Bonfim, F. Lançon, I.L. Prejbeanu, K. Mackay, B. Dieny, J. Phys. D, Appl. Phys. 46 (2013) 345308.
[55] D. Tripathy, A.O. Adeyeye, J. Appl. Phys. 105 (2009).
[56] A. Luo, F. Ma, Y. Hu, J. Magn. Magn. Mater. 413 (2016) 108–114.
[57] G.V. Swamy, H. Pandey, A.K. Srivastava, M.K. Dalai, K.K. Maurya Rashmi, R.K. Rakshit, AIP Adv. 3 (2013) 072129.
[58] D.J. Kim, J.Y. Bae, W.C. Lim, K.W. Kim, T.D. Lee, J. Appl. Phys. 101 (2007) 09B505.
[59] J. Hayakawaa, S. Ikeda, Y.M. Lee, F. Matsukura, H. Ohno, Appl. Phys. Lett. 89 (2006).
[60] S. Cardoso, P.P. Freitas, Z.G. Zhang, P. Wei, N. Barradas, J.C. Soares, J. Appl. Phys. 89 (2001) 6650–6652.
[61] A.T.G. Pym, A. Lamperti, S. Cardoso, P.P. Freitas, B.K. Tanner, Superlattices Microstruct. 41 (2007) 122–126.
[62] K. Wang, Z. Xu, Y. Huang, Y. Qiu, S. Dong, Sci. Chin. Mater. 59 (2016) 639–647.
[63] A. Gupta, S. Mohanan, M. Kinyanjui, A. Chuvilin, U. Kaiser, U. Herr, J. Appl. Phys. 107 (2010) 093910.
[64] K.W. Lin, T.J. Chen, J.Y. Guo, H. Ouyang, D.H. Wei, J. Van Lierop, J. Appl. Phys. 105 (2009) 07D710.